MATERIALS CHEMISTRY FRONTIERS

RESEARCH ARTICLE

View Article Online
View Journal | View Issue

Check for updates

Cite this: *Mater. Chem. Front.*, 2023, 7, 881

Deciphering the role of functional synergy in a catalytic molecular assembler: a proof of concept for boosted catalysis *via* retrosynthetic linker scissoring†

Ranadip Goswami,[abc] Arun Karmakar,‡[ad] Sonal Rajput,‡[b] Manpreet Singh,[ab] Subrata Kundu*[ad] and Subhadip Neogi*[ab]

Received 15th November 2022,
Accepted 13th January 2023

DOI: 10.1039/d2qm01177h

rsc.li/frontiers-materials

Artificial catalytic machinery enables improvising purpose-driven pore functionality engineering in metal–organic frameworks (MOFs) in pursuit of renewable energy sources and biomimetic hydrogen-bond-donating (HBD) organo-catalysis. Though challenging, systematic functional-tagging *via* bottom-up Lego® chemistry in such materials is highly sought and obligates a coherent design principle of self-assembly to resolve these alarming issues. We demonstrate a unique linker scissoring strategy to develop an ultra-robust MOF with redox-active Co(II) nodes from electroactive and H-bond operative struts, which exemplifies the unprecedented alliance of bimodal sustainable catalysis *via* tandem functionality installation over a single, multifaceted platform. The framework displays highly efficient and durable oxygen evolution reactions (OERs) in alkaline media with notable electrocatalytic parameters that rank among the best-known MOFs and even outperforms some benchmark catalysts. This microporous vessel further delineates the rarest $-NH_2$-hook-mediated recyclable Friedel–Crafts alkylation of indole and β-nitrostyrene *via* mild-condition HBD reactions and exhibits molecular-dimension-mediated size selectivity. The synergistic involvement of facile charge transfer in electrochemically dynamic linkers and favourable two-point H-bonding in pendent ligands underpins individual catalytic efficiency as elaborated *via* analyte-induced concomitant fluorescence modification and variable control experiments. Significantly, the key roles of task-specific sites in both OERs and HBD catalysis are validated from juxtaposing the performance of three isostructural Co(II) MOFs *via* the cooperative functional assembly of retrosynthetically fragmented MOFs. This novel strategy of sequential trimming of the functional backbone comprehensively demonstrates the superiority of the present system and leads to devising a unique catassembler as a blueprint of futuristic molecular machines for improved catalytic direction.

Introduction

Adaptable catalytic outputs *via* functionality fuelling around a supramolecular motif gave birth to modern artificial molecular machinery that mimics the natural controlling strategy of catalysis *via* a man-made multicomponent host to synergistically perform vital tasks.[1–3] The surging potential of catalytic machines instigated researchers to alleviate the self-conformable design strategy that underpins effective deciphering in globally demanding issues. For instance, incessant upsurge of energy consumption coupled with depletion of limited fossil fuels has directed researchers to search for sustainable and environmentally friendly alternative energy sources.[4] Currently, electricity-driven reactions for the development of hydrogen evolution reactions (HERs) and oxygen evolution reactions (OERs) have emerged as the most prominent tactic to convert electricity into chemical energy.[5–8] Nonetheless, the OER at the anode has sluggish kinetics due to multi-step electron transport routes, requiring additional energy to overcome the reaction energy barrier.[9] Though iridium and ruthenium oxide are utilized as benchmark OER catalysts in several avenues, their low stability, high price, and scarcity led

---

[a] *Academy of Scientific and Innovative Research (AcSIR), Ghaziabad 201002, India. E-mail: subrata_kundu2004@yahoo.co.in, sneogi@csmcri.res.in*
[b] *Inorganic Materials & Catalysis Division, CSIR-Central Salt and Marine Chemicals Research Institute (CSIR-CSMCRI), Bhavnagar, Gujarat 364002, India*
[c] *Department of Applied Chemistry and Environmental Science, School of Science, RMIT University, Melbourne, Victoria 3001, Australia*
[d] *Central Electrochemical Research Institute (CSIR-CECRI), Karaikudi, Tamil Nadu 630003, India*

† Electronic supplementary information (ESI) available: Materials and physical measurements, additional structural figures, crystal data, TGA data, PXRD patterns, FT-IR spectra, XPS, UV and fluorescence spectra, NMR spectra, and tables (PDF). CCDC 2191473. For ESI and crystallographic data in CIF or other electronic format see DOI: **https://doi.org/10.1039/d2qm01177h**

‡ These authors contributed equally.

researchers finding stable, and cost-effective metal-based systems that involve favorable conductance, hierarchical pore structure, and functional active sites.[10–12]

As a branch of crystalline porous materials, metal–organic frameworks (MOFs) received momentous attention because of their three-dimensional (3D) spanned architectures with assorted topology, regular and adjustable pores, potential to tailorability, and diversity of metal centers as well as functional groups.[13–15] Such outstanding attributes make them promising candidates for a vast range of potential applications, including electrocatalysis.[16–18] However, certain MOFs have low electrical conductivity and electrochemical activity, while many are unstable, limiting their water splitting ability. Though dual-site mechanism, surface hydroxylation, defect creation, and lattice contraction improve the electrochemical activity in MOFs,[19–22] the intrinsic electronic activity can be surged *via* purposeful linking of metal sites and organic struts. That is why Co(II) MOFs have attracted huge research attention, as the structural topology and coordination environment greatly influence the overall activity.[23] In particular, N-functionalized struts can better control the electronic configuration of metal sites for improved electrocatalytic activity.[24,25] In alkaline media, an N-ligand containing $[Co_2(m\text{-}OH)_2(bbta)]$ revealed excess potential of 292 mV for OERs.[26] Alternatively, suitable functionalization of the MOF surface with electroactive struts critically reinforces OERs *via* facile migration of generated electrons.[27] In a parallel manner, MOFs have progressively gained importance as powerful heterogeneous catalysts, owing to the existence of task-specific functionalities that activate substrate molecules.[28,29] Moreover, their optimized channels lead to much anticipated pore-fitting-induced size selectivity. For example, significant interest in the catalytic activation of reactants *via* hydrogen-bonding interactions unquestionably developed the area of hydrogen-bond-donor (HBD) catalysis.[30–32] In particular, Friedel–Crafts (FC) alkylation between indole and β-nitro styrene attracted widespread attention due to its acute importance in the production of indole-based biologically active alkaloids.[33] In view of undesired catalyst deactivation *via* self-quenching of functional groups in homogeneous HBD reactions, integration of active sites into a MOF structure *via* uniform spatial regulation is the best possible way to evade the unproductive self-assembly.[31] However, HBD catalysis in MOFs usually suffers from high catalyst loading, extended reaction period, and multistep catalyst synthesis *via* post-synthetic modification (PSM) or post-synthetic exchange (PSE).[34] Fulfilling the criteria of efficient H-bonding capability, free $-NH_2$ functionality in MOFs can be a promising alternative to Lewis acid activation for electron-deficient $-NO_2$ substituents inside the porous cavity.[35] Such $-NH_2$-mediated six-membered cyclic hydrogen bonded motif is more favorable than eight-membered (for urea-and thio-urea) or nine-membered (for squaramides) rings.[36] On this backdrop, it is advantageous, and should be promising if the coherent self-assembly approach can be applied to fabricate a single MOF for both the electrochemical OER and HBD catalysis with optimal performances to that of contemporary analogues.[37,38] Though convincing conclusions can be reached from conspicuous growth of MOFs with matching structures and different functionalities, the *status quo* is still unprecedented because of the unfavorable binding of additional functionality with concerned metal ions.

Building on the above-mentioned rationale, we demonstrate a novel linker scissoring strategy to develop a robust MOF from the assembly of Co(II) ions with an electroactive NS (2,5-di(pyridin-4-yl)thiazolo[5,4-*d*]thiazole) linker and a H-bond operative 2-ATA (2-aminoterepthalic acid) ligand. The activated framework exemplifies the high-performance OER with electrocatalytic parameters among the best-reported values among MOF materials and outperforms the benchmark catalysts IrO_2 and Co_3O_4. Combining the merits of free $-NH_2$ groups of 2-ATA and hetero atom-decked NS linkers as H-bond operative sites,

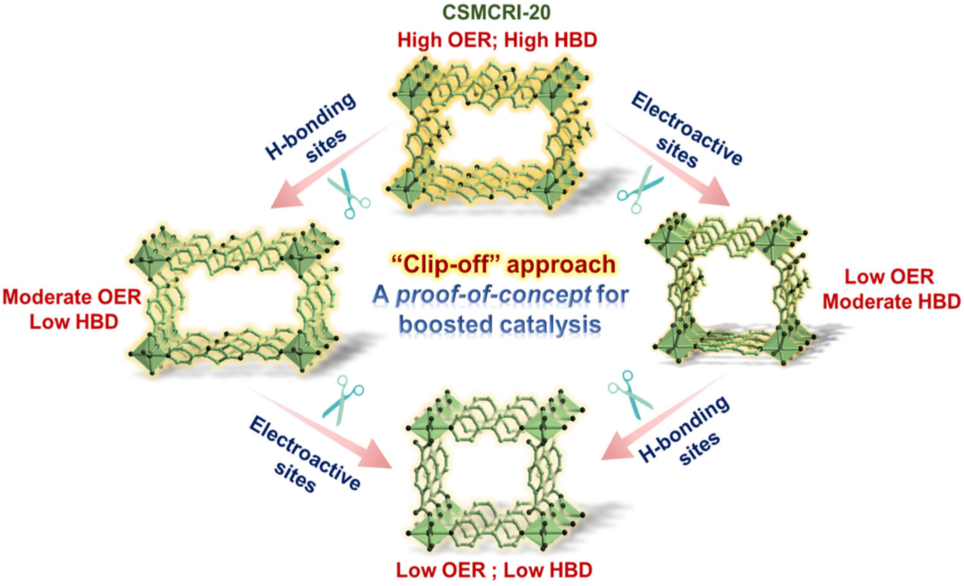

Scheme 1 Schematic illustrations of the road-map for bimodal catalysis using **CSMCRI-20** and its retrosynthetically fragmented analogues.

the framework further delineates recyclable FC alkylation *via* HBD catalysis between β-nitrostyrene and indole under mild conditions, with a broad substrate scope and unique pore-fitting-induced size selectivity.

Analyte-directed fluorescence articulation of the MOF by catalytic probes attests to guest-dependent synergistic aid of dual-functionalization towards effective electro and organo-catalysis. To articulate the role of appended functional struts in the OER and HBD catalysis, and mechanistically comprehend individual operative paths, the performance characteristics of three isostructural Co(II) MOFs are compared. The outcome led us to propose a novel molecular catassembler,[39] which allows for improved catalytic direction by a judicious and synergic functional assembly of retrosynthetically fragmented MOFs, and demonstrates a proof of concept for the progressive and futuristic catalytic machinery (Scheme 1).

Results and discussions

Crystal structure of CSMCRI-20

Block-shaped red crystals of **CSMCRI-20** (CSMCRI = Central Salt & Marine Chemicals Research Institute) revealed the orthorhombic space group *Pccn* (Table S2, ESI†). The asymmetric unit contains a Co(II) ion, 2-ATA ligand and NS linker, one each (Fig. S2a, ESI†). Every Co(II) centre exhibits a hexacoordinated N_2O_4 environment with ligation from two pyridyl nitrogen atoms (average Co–N = 2.206 Å) from different NS linkers, and four oxygen from three deprotonated 2-ATA ligands (Co–O = 1.980–2.350 Å) in chelating as well as μ_2-bridging modes. Two independent Co(II) ions are bridged by two carboxylate groups and form a binuclear $[Co_2(COO)_4]$ subunit with a Co···Co spacing of 4.032 Å. The carboxylate ligands are linked *via* these binuclear metal nodes, and form a 2D layer with a rhombus window of dimension 10.09 × 12.67 $Å^2$ (atom-to-atom connection) along the crystallographic *bc* plane (Fig. 1(a)). Noticeably, $-NH_2$ groups of 2-ATA remain free and projected inside the pore, bestowing a hydrogen-bond operative pore environment. The linear N-donor linkers are coordinated to the axial sites of each Co(II) ion and extend the 2D layer to a third dimension *via* the formation of a bipillar-layer structure (Fig. 1(b)) with large voids (11.81 × 5.39 $Å^2$). The overall framework topology is 6-c net *pcu* (Fig. S2b, ESI†) with a Schlafli symbol $\{4^{12}\cdot6^3\}$.[40] Such huge pores mutually instigate 2-fold interpenetration (Fig. 1(c)) to **CSMCRI-20** with generation of nearly rectangular-shaped voids of dimension 11.81 × 5.39 $Å^2$ (Fig. 1(d)).

The neighboring NS pillars exhibit strong π–π stacking interactions, whilst non-covalent interactions exist between the 2-ATA ligand and the NS linker. These secondary interactions equally promote the stability and integrity of the framework. The molecular formula $[Co(2\text{-}ATA)(NS)]\cdot0.5DMF\cdot1.5H_2O$ was cumulatively ascertained from the combined inputs of thermogravimetric analysis (TGA), PLATON calculation,[41] and elemental analysis.

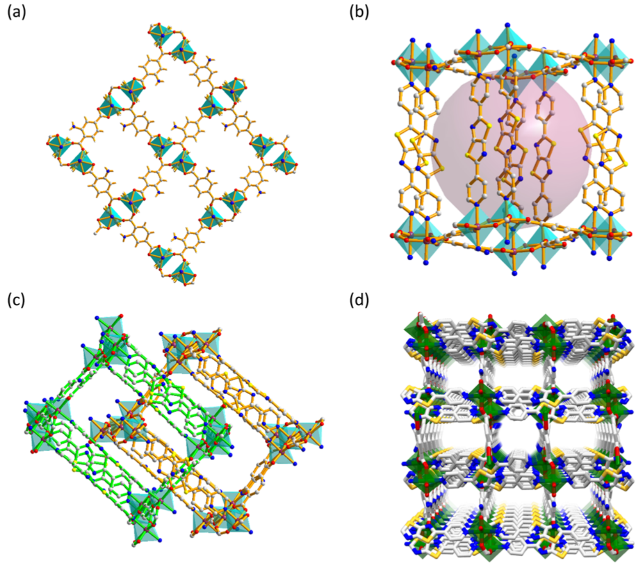

Fig. 1 (a) Two-dimensional layer of the framework along the crystallographic *ac* plane. (b) Single net void-view of **CSMCRI-20**. (c) Two-fold interpenetrated view of the framework. (d) Porous view of **CSMCRI-20** along the crystallographic *c* axis.

Structural studies and thermo-chemical stability

The bulk phase purity of **CSMCRI-20** was verified from the similarity in the powder X-ray diffraction (PXRD) pattern to that of the simulated one (Fig. S5c, ESI†). Scanning electron microscopy (SEM) and energy-dispersive X-ray (EDX) analysis divulged all anticipated elements (Co, C, N, S, and O) uniformly distributed throughout the surface of rectangular blocked-shaped crystals (Fig. 2(b)). Sharp peaks at 1650 cm^{-1} and 3280 cm^{-1} in the FT-IR spectrum are attributed to the presence of free $-NH_2$ moieties in the framework (Fig. S3a, ESI†).[42] TGA of **CSMCRI-20** in a N_2 atmosphere revealed 11.52% weight loss (calcd 10.62%) in the temperature range 30–300 °C. Framework degradation occurs after a plateau at 350 °C (Fig. S3b, ESI†). Further, variable temperature PXRD patterns confirm thermal stability up to 300 °C (Fig. S5d, ESI†). Remarkably, **CSMCRI-20** is capable of preserving its structural integrity (Fig. 2(a) and Fig. S5a, ESI†) when exposed to certain harsh conditions including boiling water, open air, 0.1 M HCl, 0.1 M and 1 M KOH, validating its chemical stability. To establish the oxidation states of the metal and chemical environment of the elements, X-ray photoelectron spectroscopy (XPS) was applied (Fig. 2(c)). Fig. 2(d) shows the high-resolution XPS spectrum of Co(II) 2p with distinctive peaks of Co $2p_{3/2}$ and Co $2p_{1/2}$ at binding energies (BEs) 780.66 and 796.45 eV, respectively.[43] Moreover, two different satellite (Fig. 2(d)) peaks for Co $2p_{3/2}$ and Co $2p_{1/2}$ are observed at 784.66 and 801.18 eV, respectively. The deconvoluted C 1s spectrum (Fig. S4a, ESI†) contains three peaks at BEs 284.32, 285.51 and 287.73 eV that corroborate C═C, C═N and C═O bonds, respectively.[44] The N 1s spectrum (Fig. S4b, ESI†) encompasses a distinctive peak at 399.22 eV, assigned to the Co–N bonding in the framework.[45] Peaks at 532.12 and 530.89 eV in the deconvoluted spectrum of O 1s

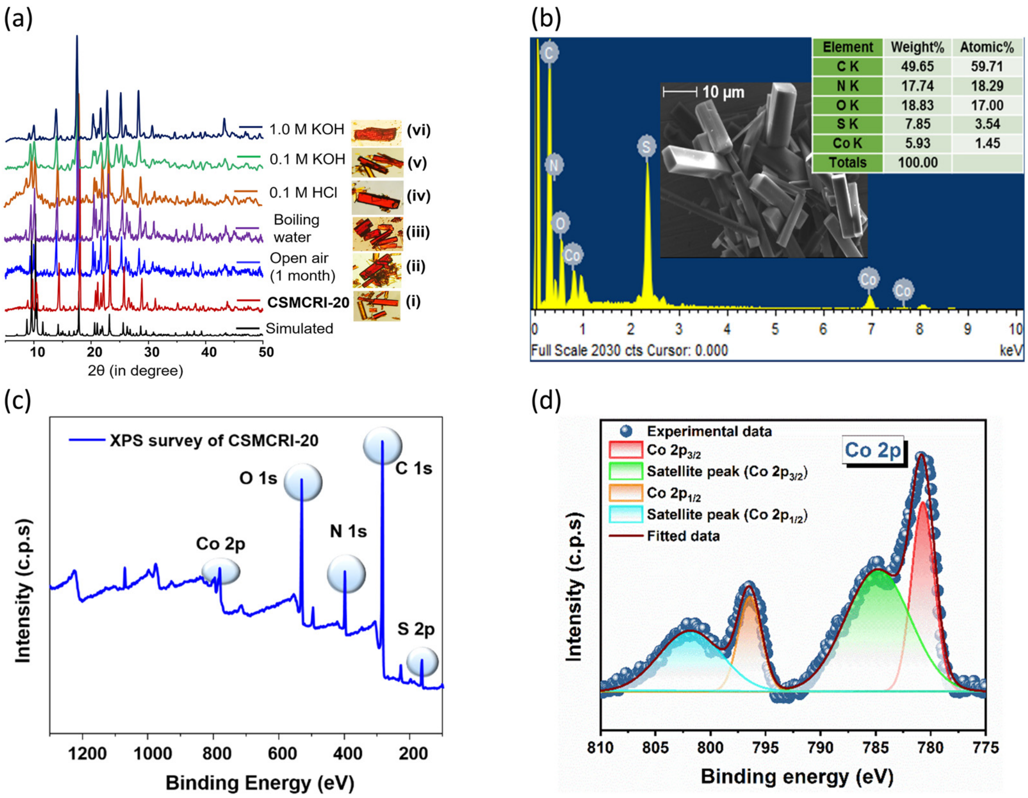

Element	Weight%	Atomic%
C K	49.65	59.71
N K	17.74	18.29
O K	18.83	17.00
S K	7.85	3.54
Co K	5.93	1.45
Totals	100.00	

Fig. 2 (a) PXRD patterns and optical images of the MOF under different experimental conditions, (i) as made **CSMCRI-20**, under (ii) open air (1 month), (iii) boiling water, (iv) 0.1 M HCl, (v) 0.1 M KOH and (vi) 1 M KOH. (b) FE-SEM image and EDX analysis of **CSMCRI-20**. (c) XPS survey spectra of the framework. (d) High-resolution XPS spectrum of Co 2p.

(Fig. S4c, ESI†) suggest the bonding of Co–O and C═O, respectively.[46] The deconvoluted S 2p spectrum (Fig. S4d, ESI†) includes characteristic distinctive peaks at 164.14 and 165.07 eV for S 2p$_{3/2}$ and S 2p$_{1/2}$ spin–orbit peaks, respectively.[42] The guest-free structure (**20a**) was obtained *via* heating the solvent-exchanged (with dichloromethane) framework at 100 °C for 4 h followed by dynamic evacuation. The maintenance of structural integrity in **20a** was validated from PXRD (Fig. S5c, ESI†), and FT-IR (Fig. S3a, ESI†) studies. The activated framework shows 40 cm^3 g^{-1} CO$_2$ gas uptake at 195 K up to 1.0 relative pressure (P/P_0) that corresponds to a Brunauer–Emmett–Teller (BET) surface area of 105.6 m^2 g^{-1} (Fig. S5e, ESI†).

Electrocatalytic water oxidation

Surmising on the co-existence of redox-active Co(ɪɪ) centres, electrochemically dynamic NS linker, and free –NH$_2$ sites, we checked the electrochemical oxygen evolution reaction (OER) in the MOF. The OER experiment was studied in 1 M KOH solution (electrolyte) using **20a** as the working electrode. Carbon cloth and Hg/HgO acted as the counter and reference electrodes, respectively. Linear sweep voltammetry (LSV) was achieved in the potential range of 1–2 V (*vs.* RHE) under a ‘Fe free’ condition (at pH = 13.8) at a low scan rate of 5 mV sec^{-1} to discard interference from capacitive currents. Fig. 3(a) divulges that 391 mV overpotential (η) is required to attain a standard current density of 10 mA cm^{-2}, as evidenced from 75% iR rectified LSV polarization curve of **20a**. The overpotential value is bit higher than that of the commercially available benchmark electrocatalyst RuO$_2$ (370 mV), but significantly lower than that of Co$_3$O$_4$ (430 mV) as well as prevailing Co(ɪɪ)-based frameworks (Fig. 3(a) and Table S4, ESI†). To gain deeper insights into the electron transfer kinetics at the electrode–electrolyte interface, Tafel plots[47] were extracted from the LSV study. Fig. 3(b) describes a Tafel slope value of 85 mV dec^{-1}, which infers a superior charge transfer ability of **20a** to commercial Co$_3$O$_4$ (92 mV dec^{-1}),[48] IrO$_2$ (100.47 mV dec^{-1})[49] and many other MOF electrocatalysts (Table S4, ESI†). Moreover, the value is comparable to the state-of-the-art catalyst RuO$_2$ (74 mV dec^{-1}) in the lower overpotential region.[50] LSV polarization curves from rapid recycling of the catalyst *via* accelerated degradation (AD) for 1000 cycles (scan rate: 150 mV s^{-1}) showed minimum alternation in the overpotential ($\sim$28 mV) before and after cycling (Fig. 4(a)). This outcome suggests minimal deterioration in electrochemical activity and supports enduring nature of the framework. Further, trivial deviation of current density in the *j–t* curve of chronoamperometric measurement without iR assistance for 15 h (Fig. 4(b)) verified this fact. Moreover, pH-dependent OER studies (Fig. S9, ESI†) showed increased performance with the increase in concentration of KOH solution, and points that O$_2$ evolution is proportionally boosted as a result of maximising the number of OH$^-$ ions to the catalyst surface.[43,51] Moreover, the Nyquist plot apprises a lower charge transfer resistance (R_{ct}) value (4.44 Ω) for **20a** when compared with RuO$_2$ (6.03 Ω) and Co$_3$O$_4$ (7.01 Ω). This

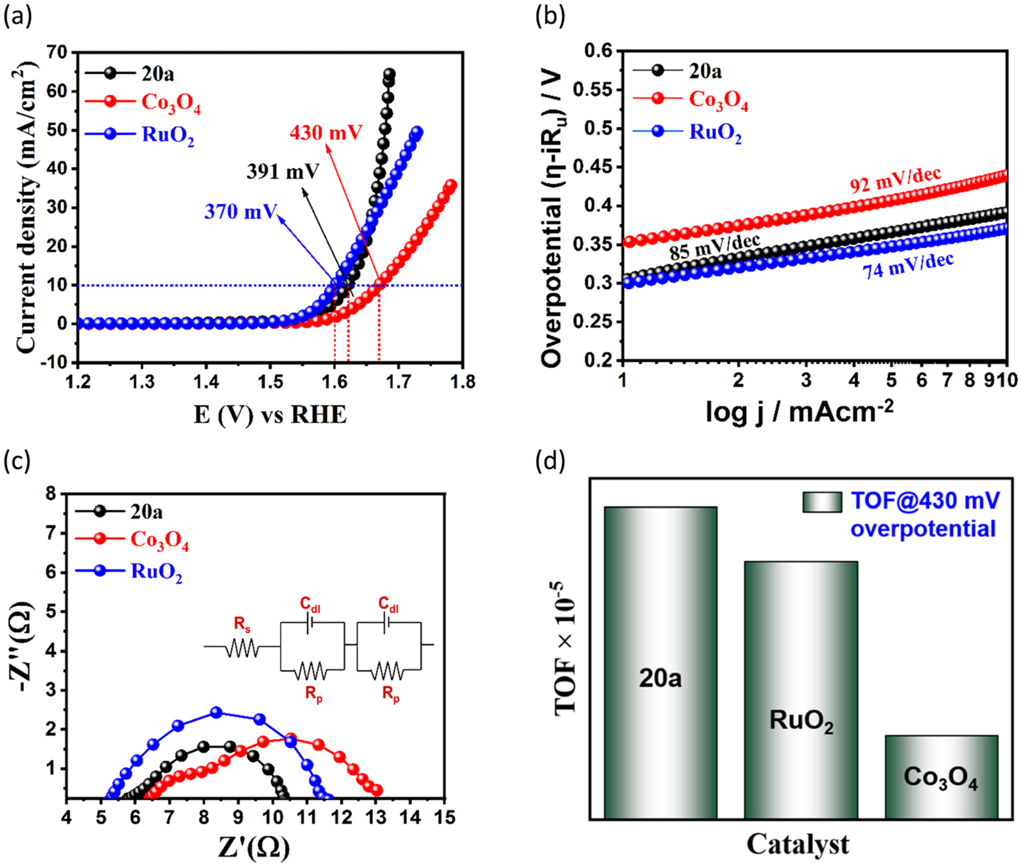

Fig. 3 (a) Linear sweep voltammetry (LSV) for the present MOF and other benchmark commercial electrocatalysts. (b) Tafel plot for activated **CSMCRI-20**. (c) Electrochemical impedance spectra (EIS) of **20a** at 10 mA cm^{-2}. (d) Turn-over frequency (TOF) values for **20a**, RuO_2 and Co_3O_4.

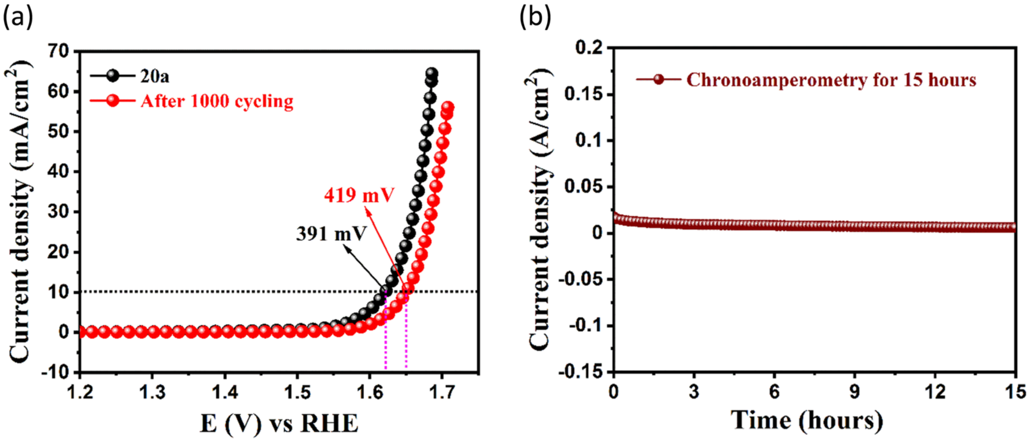

Fig. 4 (a) LSV for activated **CSMCRI-20** and after 1000 cycles showing trivial deviation in overpotential. (b) Chronoamperometric study of **20a** performed at 10 mA cm^{-2} for 15 h.

observation implies enhanced feasibility of electron transfer for **20a** (Fig. 3(c)) with lower resistance values especially at escalated overpotentials and corroborates this MOF as a high-performing electrocatalyst. Appreciable faradaic efficiency (94.6%) also justifies the electrocatalytic significance of this OER catalyst (Fig. S6, ESI†). The inherent catalytic activity of **20a** was further evaluated from key characteristics parameters such as electrochemically active surface area (EASA), roughness factor (R_f) and turnover frequency (TOF). EASA was calculated using electrochemical double layer capacitance (C_{dl}) generated *via* charge accumulation at the non-faradaic region and specific capacitance of a flat surface of the working electrode (C_s).

A decent linear fit was obtained from the CV plot between different scan rates with current density, and the slope of the aforesaid plot (C_{dl}) turned out to be 0.0906 mF for **20a** (Fig. S8, ESI†). Based on the conventional specific capacitance (C_s) value of 0.040 mF cm^{-2}, EASA was calculated to be 2.4 cm^2, which entails highly interactive and exposed surface area of the electrocatalyst.

Further, R_f was derived from the ratio of EASA to geometrical surface area of the working electrode (0.5 cm^2) and found to be 4.8. It is worth mentioning that TOF (4.03×10^{-4} s^{-1}) for **20a** at 430 mV overpotential outperforms the corresponding values of commercially used benchmark OER catalysts Co_3O_4 (2.46×10^{-5} s^{-1}) and RuO_2 (7.57×10^{-5} s^{-1}) (Fig. 3(d)). Notably, the mass activity of the MOF also followed the identical trend with surface area, which was confirmed by comparing the mass activity normalized LSV curve with the surface area normalized LSV curve (Fig. S10, ESI†). In view of long-term electrocatalytic durability of the material, post-OER intactness of the framework was verified from XPS measurement (Fig. S12, ESI†), PXRD and surface area (Fig. S13, ESI†) analysis, which revealed conserved patterns and/or peak intensities with unaltered block-shaped morphology (Fig. S11, ESI†). In addition, inductively coupled plasma-optical emission spectroscopy (ICP-OES) analysis revealed no leaching of the Co^{2+} ions and ruled out any possibility of metal leakage during OER cycling.

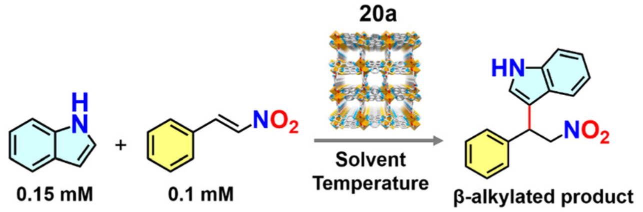

Scheme 2 Model reaction between β-nitrostyrene and indole, catalysed by **20a**.

Hydrogen-bond-donating recyclable Friedel–Crafts alkylation with size selectivity

Hydrogen-bond-mediated organo-catalytic activity of guest-free **CSMCRI-20** in Friedel–Crafts (FC) alkylation was studied using 1*H*-indole (0.15 mmol) and (*E*)-(2-nitrovinyl)benzene (β-nitrostyrene) (0.1 mmol) as model substrates (Scheme 2). The conversion of products was analysed by ^{1}H NMR spectroscopy. This hydrogen-bond donor (HBD) catalysis in various low-polar solvents displayed the highest yield of the product in dichloromethane (DCM) (Fig. 6(a) and Table S1, ESI†). However, the maximum yield of 3-(1-nitro-2-phenylethyl)-1*H*-indole (Scheme 2) was observed at 60 °C, which is still below that of the majority of MOF-based FC alkylation reports (Table S5, ESI†).

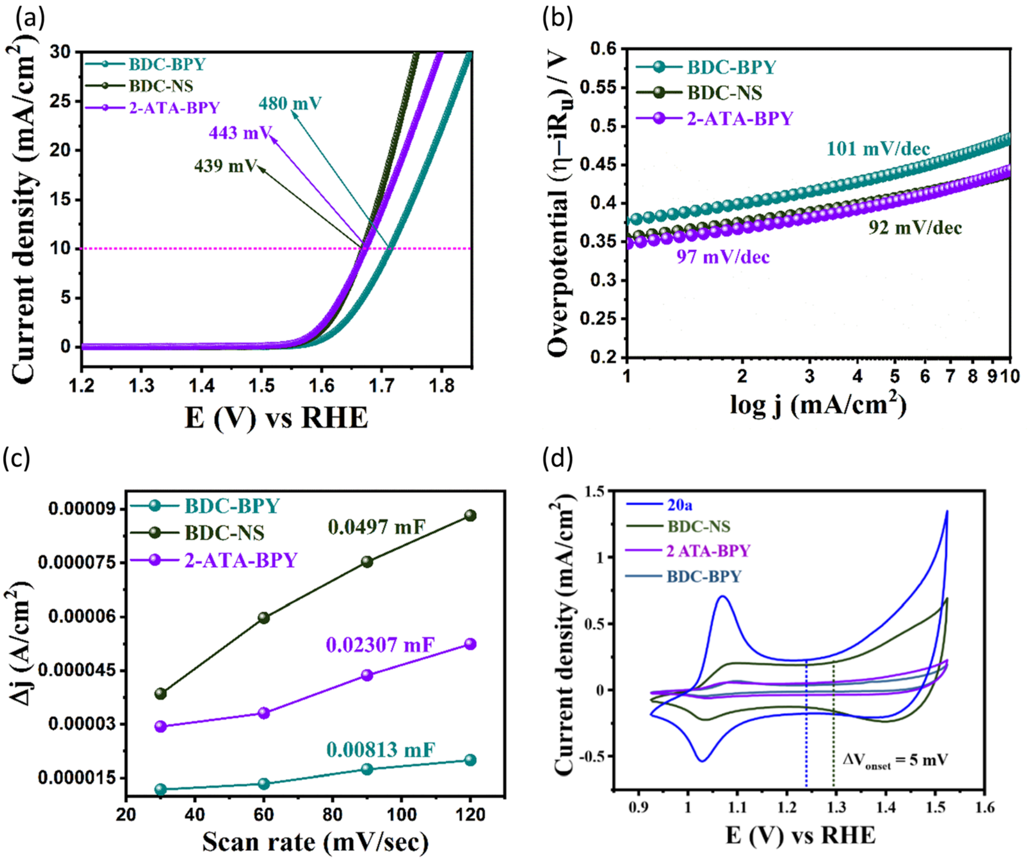

Fig. 5 (a) LSV curve for BDC-BPY (BDC: benzene-1,4-dicarboxylic acid, BPY: 4,4′-bipyridine), BDC-NS and 2-ATA-BPY. (b) Tafel plot for BDC-BPY, BDC-NS and 2-ATA-BPY. (c) EASA values and (d) cyclic voltammogram (CV) for three Co(II) MOFs.

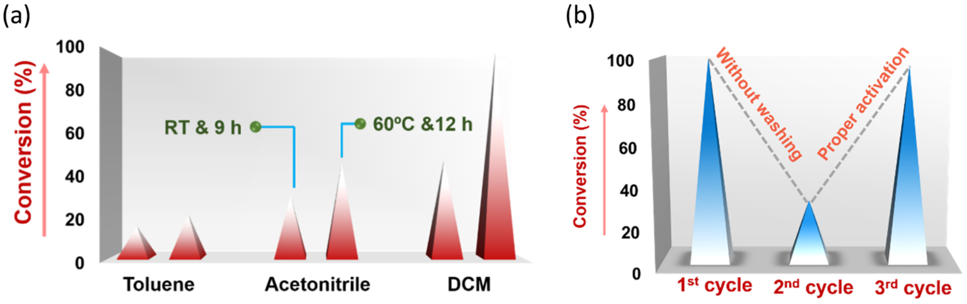

Fig. 6 (a) Effect of solvent and temperature on the conversion (%) of HBD reaction. (b) Conversion (%) of the product without and with proper activation of the catalyst.

Reaction time optimization revealed maximum conversion of the product at 12 h, while variation of catalyst loading from 5 mol% to 9 mol% showed an obvious improvement in the product yield from 77.5 to 100%. Thus, the optimum reaction condition to attain maximum yields of the product was fixed as 60 °C for 12 h by 9 mol% of **20a** in DCM (Table S1 and Fig. S14, ESI†). The heterogeneous nature of **20a** was established from the leaching experiment. For this, the catalyst was separated after the completion of reaction, and ICP-OES of the remaining mixture revealed no presence of Co(II) ions. In a separate experiment, progress of HBD catalysis was checked after 6 h, and the dispersed catalyst was removed *via* filtration. No further conversion of nitroalkylated indole upon continuing the reaction (Fig. S30, ESI†) validates that **20a** is compulsory for the reaction to progress. To validate the impact of specific functionality in HBD catalysis, the reaction was tested using diverse catalyst combinations including the as-made MOF (**CSMCRI-20**), without catalyst, and individual/mixture of MOF components under optimized conditions. As described in Table 1 (entry 1), no conversion was attained using $Co(NO_3)_2\cdot 6H_2O$, and discards any role of metal centres in the FC alkylation reaction. However, the catalyst-free condition (Table 1, entry 7) did not produce any yield, whilst **CSMCRI-20** divulged 26% conversion (Table 1, entry 3). Conversely, 2-ATA and NS struts individually provided moderate product conversion (Table 1, entries 2 and 4) owing to the presence of H-bonding sites for substrate activation.[35] In contrast, a combined mixture of organic struts showed less conversion (Table 1, entry 5) that might stem from the intermolecular hydrogen-bonding-induced self-quenching between free $-NH_2$ groups of 2-ATA and the hetero-atom-decked NS linker. This phenomenon was reaffirmed *via* optical fluorescence quenching of aqueous

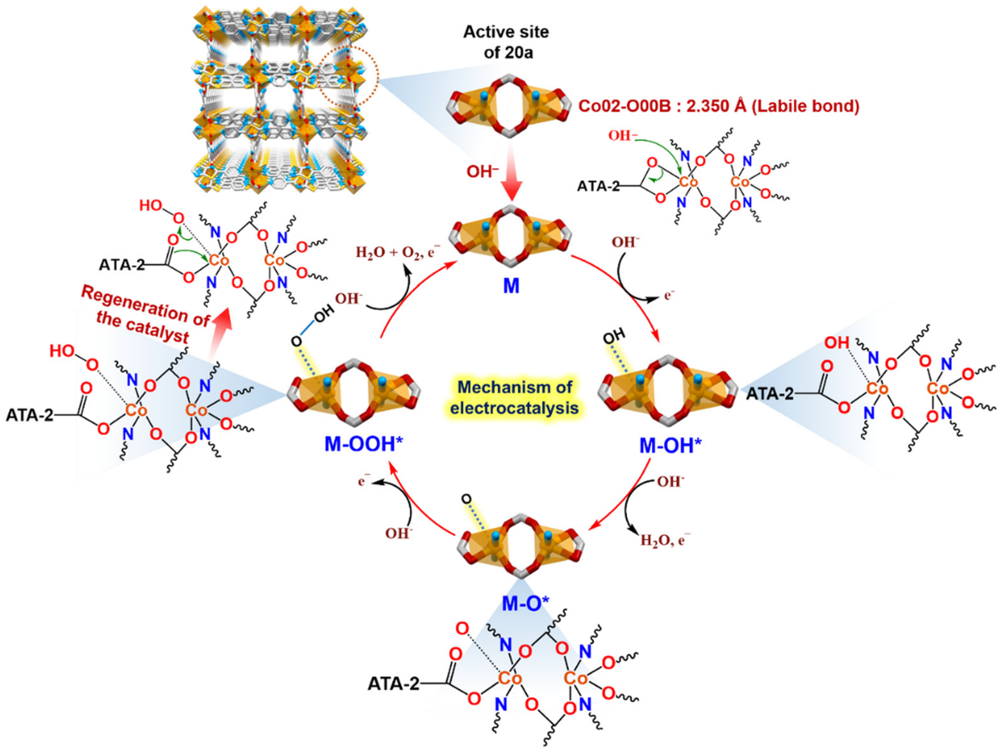

Fig. 7 Plausible mechanistic pathway for the OER kinetics by activated **CSMCRI-20**.

Table 1 Optimization of catalysts for the Friedel–Crafts alkylation reaction between indole and β-nitrostyrene

Entry	Catalyst	Catalyst (mol %)	Time (h)	Solvent	Temp (°)	Conversion[a] (%)
1.	$Co(NO_3)_2{\cdot}4H_2O$	9	12	DCM	60	—
2.	2-ATA	9	12	DCM	60	52
3.	**CSMCRI-20**	9	12	DCM	60	26
4.	NS	9	12	DCM	60	34
5.	2-ATA + NS	9	12	DCM	60	45
6.	**20a**	9	12	DCM	60	100
7.	Blank	9	12	DCM	60	—
8.	BDC-NS	9	12	DCM	60	50
9.	2-ATA-BPY	9	12	DCM	60	66
10.	BDC-BPY	9	12	DCM	60	24

[a] Determined from ^1H NMR spectroscopy.

solution of 2-ATA in the presence of the NS linker (Fig. 8(b) and (c)). In a nutshell, suitably grafted task-specific functionalities in the MOF backbone synergistically govern this HBD catalysis, wherein spatially controlled arrangements of $-NH_2$ groups in 2-ATA and the hetero-atom-decked NS linker influenced the operative non-covalent interactions with the reactants. To more explicitly support this verdict, and further elucidate functionality-induced catalytic evolution, indole alkylation reactions in the presence of isoreticular MOFs were deliberated (*vide infra*).

Catalyst recyclability was checked by isolating **20a** from the reaction mixture, followed by washing with DCM and drying at 100 °C for 4 h. The regenerated catalyst revealed trivial loss in activity up to five catalysis-recovery cycles (Fig. S29, ESI†). Further, FE-SEM analysis (Fig. S26, ESI†) divulged the unaltered block-shaped morphology of the recycled catalyst, while the PXRD pattern of the reused **20a** (Fig. S27, ESI†) showed complete maintenance of crystallinity and peak positions. Besides, XPS analysis showed similar spectral pattern to that of pristine MOF along with the presence of all constituting elements, corroborating intactness of the organo-catalyst (Fig. S28, ESI†).

We checked the catalytic efficiency of substituted indoles to acquire insights into the reactivity of the C-3 centre. Though electron-rich 7-methyl indole assists in the activation of the indole ring for nucleophilic attack, less product conversion (68.1%) necessarily points to the steric factor (Table 2, entry 2). However, 5-chloro and 5-cyano indoles divulged 68.6% and 24.2% conversion (Table 2, entries 3 and 4), respectively, due to the progressive electron-withdrawing nature and steric effect, which reduce the nucleophilicity of the indole ring for further attack. To establish simultaneous effects of electronic and steric factors on catalytic transformation, fluoro- and carboxylic acid-substituted indoles were considered, which furnished no products at all (Table 2, entry 7).[31] While the model substrate with a molecular dimension of 5.0 × 6.58 Å can facilely diffuse through the pore-channels of **20a**, 7-benzoyloxy indole surprisingly leads to 23.2% conversion (Table 2, entry 5) *via* surface catalysis, because of its larger molecular dimension (11.34 × 6.61 Å). Additional experiments with this bulky indole using a longer reaction time did not cross the product yield 25% (Table 2, entry 8), and points that this particular indole derivative finds trouble in diffusing through the pore aperture of the two-fold interpenetrated framework and interacting with H-bonding sites.

To further elaborate such pore-mediated size-excusive HBD catalysis, we reused the catalyst without washing and/or proper activation after initial run, and found only 35% conversion. Strikingly, thoroughly washed and properly activated **20a** regained its usual catalytic efficiency in the subsequent cycle as a result of revival of the porous structure, which benefits the reaction to occur inside the MOF channel. The effect of substituents on β-nitro styrene in HBD catalysis was demonstrated considering *trans*-4-methoxy-β-nitrostyrene (Table 3, entry 3) and its chloro-substituted analogue (Table 3, entries 2 & 5), which showed excellent performance. However, methylated β-nitrostyrene displayed reduced catalytic performance (Table 3, entry 4). These variations are attributed to various electronic effects of the functional groups on the aromatic ring of the nitrostyrene moiety, wherein reduction in electrophilicity by $-CH_3$ diminishes the tendency to activate the $-NO_2$ group towards facile H-bonding interactions.

Mechanistic validation of the electrochemical OER and HBD catalysis

Cyclic voltammetry of **20a** revealed two redox peaks at 1.1 and 1.38 V, ascribed to the NS linker and $Co^{2+} \rightarrow Co^{3+}$ oxidation (Fig. S7, ESI†), respectively. Primarily, intermolecular H-bonding between free $-NH_2$ from 2-ATA and OH^- ions assist in diffusing smaller sized OH^- ions through the porous channels in the framework.[52,53] Such possibility of H-bonding aided ion diffusion was proven through obvious fluorescence quenching of the framework upon addition of 1 mM KOH solution (Fig. 8(c)). Besides, the NS linker generates electronic charge, which efficiently facilitates charge transfer activity in the MOF, as validated from sharp luminescence enhancement of **20a** in the subsequent presence of aromatic guest naphthalene (Fig. 8(c)). Then again, the weakly chelated carboxylate group around densely packed metal centres in the 3D structure can be disrupted by strong nucleophile OH^- to act as Lewis acidic sites without disturbing the overall structure.[54] Principally, the alkaline OER proceeds *via* generation of the following metal intermediates:

$$M + OH^- \rightarrow M - OH^* + e^-$$

$$M - OH^* + OH^- \rightarrow M - O^* + H_2O + e^-$$

$$M - O^* + OH^- \rightarrow M - OOH^* + e^-$$

$$M - OOH^* + OH^- \rightarrow M + O_2 + H_2O + e^-$$

Several active site-adsorbed intermediates (here metal, M is the active site) are formed by the generation of four electrons, which finally produce O_2 molecule *via* regeneration of the pristine Co(II) site.[55,56] At the onset, hydroxide ions attack the Co(II) metal centre as a result of dissociation of the weakly chelated Co02–O00B bond (bond length 2.350 Å), forming M–OH* species. Rapid removal of the H_2O molecule in the

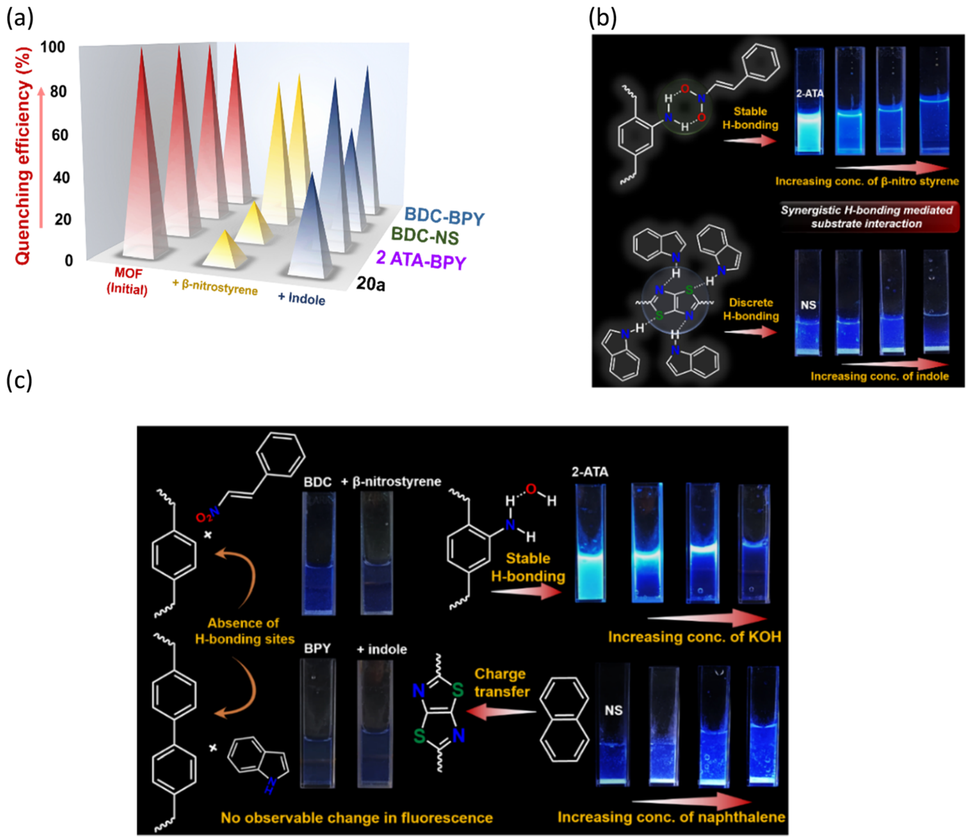

Fig. 8 (a) Change in the luminescence intensity of four Co(II)-based frameworks upon gradual addition of β-nitrostyrene and indole. (b) Optical evidence of synergistic H-bonding-mediated substrate interaction in HBD catalysis. (c) Luminescence modulation in mono- and non-functionalized Co(II) MOFs *via* interaction of substrates of HBD catalysis and synergistic influence of 2-ATA and NS for OER activity.

following step produces a M–O* intermediate, which, in turn, forms a metal–oxyhydroxide (M–OOH*) intermediate *via* the simultaneous attack of the third OH^- group. In the last step, the fourth OH^- group extracts a proton from the M–OOH* species to release a H_2O molecule, while the O_2 molecule is detached from the metal centre with the regeneration of a catalytically active parent motif (Fig. 7).

Alternatively, we investigated the mechanistic aspects of HBD catalysis-mediated FC alkylation from the combined inputs of control experiments and previous reports in the literature.[36] For clarity, a smaller unit of **CSMCRI-20** containing $-NH_2$ hooked 2-ATA and heteroatom-linked NS linkers was considered (Fig. 9). In the first step, six-membered H-bonded ring forms between $-NH_2$ of 2-ATA and $-NO_2$ of the electrophile that is principally more favorable than higher numbered rings containing H-bonded motifs (as in case of urea/thiourea/squaramide-functionalities).[35] Such H-bonding interactions eventually enhance the electrophilicity of the carbon atom and facilitate attacks from the C-3 centre of indole. To verify such interaction, we conducted a fluorescence titration experiment using MOF dispersion (2 mg of **20a** in 2 mL DCM) with the incremental presence of a β-nitrostyrene solution (1 mM in DCM). Pristine emission intensity of the MOF rapidly quenched (95%) upon successive addition of β-nitrostyrene (20 μL each time), pointing to the formation of effective H-bonding *via* electronic communication by the $-NO_2$ group in the immediate vicinity of the primary amide side arm (Fig. 8(a) and (b)). In a distinctive experiment, HBD catalysis of 5-fluoro-1*H*-indole-2-carboxylic acid was targeted, which did not proceed with the model electrophile (Table 2, entry 7). This phenomenon is ascribed to the strong interaction between the carboxylic acid group in the substrate and the primary amide moiety, which leaves no place to interact with the $-NO_2$ group, and otherwise authenticates two-point H-bonding. In a similar manner, addition of indole (1 mM in DCM) also reduced the luminous MOF intensity owing to the facile H-bonding interaction with bare hetero-atoms from the NS linker (Fig. 8(a) and (b)). In the ensuing steps, the attack from the C-3 centre of indole to the α-carbon atom of β-nitrostyrene results in C–C bond formation, and the expected product is formed *via* concerted rearrangement and hydrogen transfer steps. Finally, release of products regenerates the MOF catalyst for participation in the next catalytic cycle (Fig. 9).

Molecular catassembler: a proof of concept for boosted catalysis *via* retrosynthetic dysfunctionalization

Building on the importance of judicious positioning of reactive sites on the MOF backbone to direct an effective catalytic pathway, we envisaged one of the pioneering concepts of molecular assemblers,[57] guided by four sequential thumbs: (1) recognition and binding of the reactants; (2) orientation of

Table 2 Substrate scope in the Friedel–Crafts alkylation reaction with indoles using **20a**

Sl. no.	Reactant	Model structure	Product	Conversion[a] (%)	TON[b]
1.	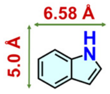	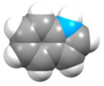	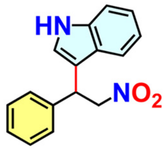	100	10.68
2.		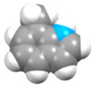	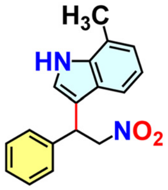	68.1	7.26
3.	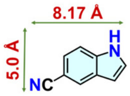	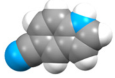	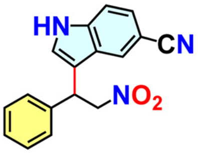	24.2	2.56
4.	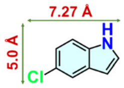	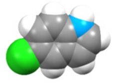	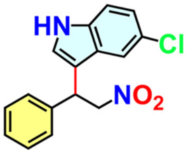	68.6	7.32
5.		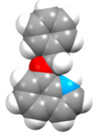	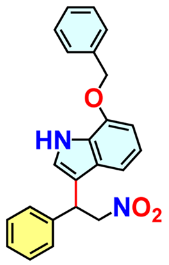	23.2	2.47
6.	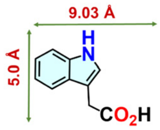	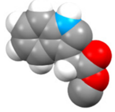	No reaction	—	—
7.	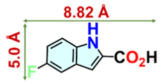	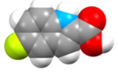	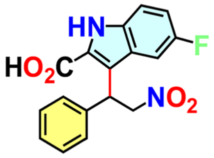	—	—
8.		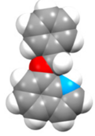	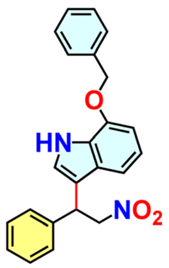	25.1[c]	2.63

[a] Determined by ^{1}H NMR spectroscopy. [b] Number of moles of product per mole of the catalyst. [c] Reaction duration of 24 h.

the reactants with atomic precision; (3) catalysed bond formation, and (4) active release of the product and repeating the cycle.[39] Apart from the basic aspects of single molecular assemblers, "molecular catassembler" was coined by Tian etal.,[58] referring to a molecular assembly that boosts particular catalytic reactions *via* providing reactive binding sites. As a

Table 3 Substrate scope in the Friedel–Crafts alkylation reaction with varied β-nitrostyrenes using **20a**

Sl. no.	Reactant	Model structure	Product	Conversion[a] (%)	TON[b]
1.	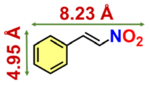	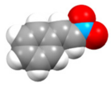	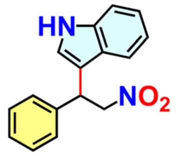	100	10.68
2.	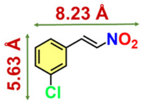	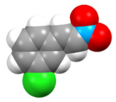	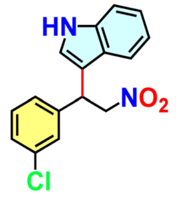	67.5	7.20
3.	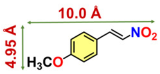	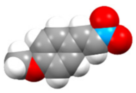	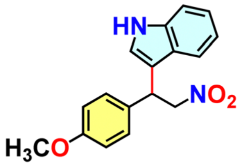	66	7.04
4.	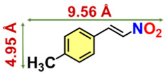		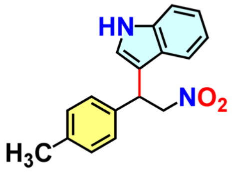	76.83	8.11
5.	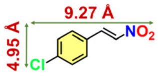	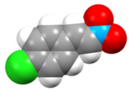	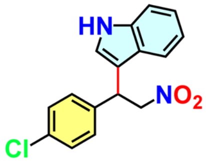	91.44	9.71

[a] Determined by ^1H NMR spectroscopy. [b] Number of moles of product per mole of the catalyst.

proof of concept to examine catalytic evolution in **20a** *via* the stepwise retrosynthetic disassembly of task-specific sites, we chose three isostructural Co(II) MOFs: BDC-NS; 2-ATA-BPY and BDC-BPY (Fig. 10, 11 and Fig. S2, ESI†).[59–61] First, we observed the OER variation in these MOFs *via* successive trimming of the side-chain functionalization in 2-ATA as well as heteroatom-fused heterocyclic rings of the NS linker. While BDC-BPY requires 480 mV of overpotential to achieve 10 mA current density, BDC-NS and 2-ATA-BPY demand 439 mV and 443 mV overpotential, respectively (Fig. 5(a)). Further, both Tafel (Fig. 5(b)) slopes (BDC-NS: 92 mV dec^{-1}; 2-ATA-BPY: 97 mV dec^{-1} and BDC-BPY: 101 mV dec^{-1} respectively) and EASA values (Fig. 5(c)) are in complete harmony with functionality-dependent overpotential. Given that the synergistic presence of the redox-active NS linker and $–NH_2$-hooked ligand facilitates effective charge conduction as well as oxidation of metal ions during the formation of the M–OOH* intermediate (*vide supra*), the unavailability of both the sites in non-functionalized BDC-BPY resulted in the lowest OER performance. In fact, mono-functionalized BDC-NS (pillar functionalization) and 2-ATA-BPY (layer functionalization) showed inferior performance to **20a**, which is also reflected from individual cyclic voltammogram (Fig. 5(d)).

To next elaborate the impact of stepwise retrosynthetic disassembly on operative H-bonding interactions for the HBD reaction (Fig. 10), we checked the organo-catalytic performance of these MOFs under the aforesaid optimized conditions, and compared with **20a**. As portrayed in Tables 1, 2-ATA-BPY furnished 66% conversion (entry 9) because the favourable primary-amine functionality triggered two-point H-bonding, while BDC-NS achieved a lower yield of 50% due to the presence of the NS linker, which forms less-active discrete H-bonding interaction with the H-atom of indole by one of the heteroatoms (Table 1, entry 8). To rationalize the synergistic substrate activation *via* dual-site H-bonding interactions, HBD catalysis was extended using non-functionalized BDC-BPY that hardly yields any product (Table 1, entry 10) and certifies mutual operation of H-bonding sites in the most active catalyst **20a**. In a nutshell, the essential features of a molecular catassembler including purpose-driven substrate recognition sites and self-releasable nature with high yield are met, which undoubtedly makes this MOF a potential candidate for synergistic catalysis, proven *via* the descending mode of catalytic machinery.

Conclusions

Surmising the importance of judicious positioning of multiple reactive sites onto MOF backbones to direct effective catalytic

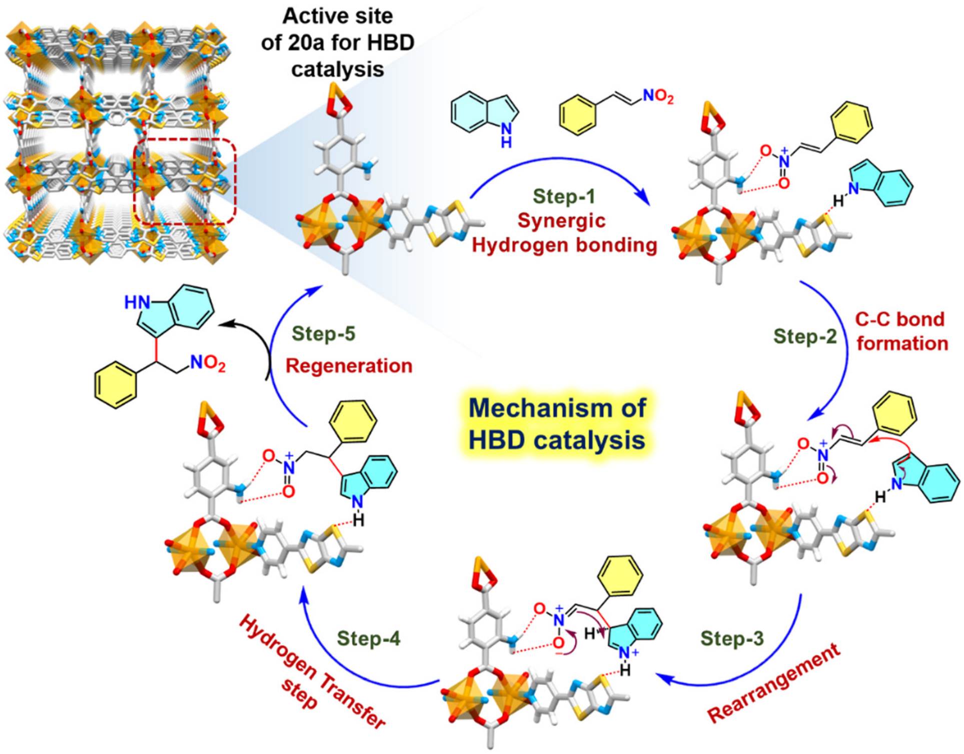

Fig. 9 Plausible H-bonding-mediated reaction mechanism for the FC alkylation reaction of indole with β-nitrostyrene by **20a** (partial view of the framework is presented for clarity).

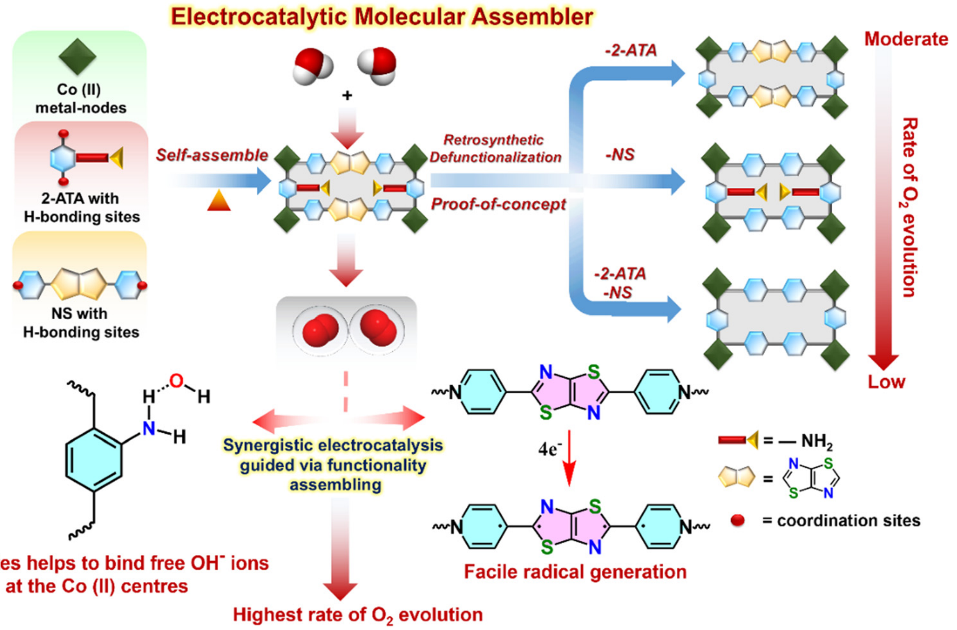

Fig. 10 Schematic illustration of the electrocatalytic molecular catassembler as a proof of concept for boosted O_2 generation.

pathways, we fabricated a microporous Co(II) framework from incisive amalgamation of a H-bonding operative ligand, a hetero-atom-appended electroactive strut and redox-active $[Co_2(COO)_4]$ subunit that exhibits high thermo-chemical robustness. The activated framework exemplifies highly efficient oxygen evolution reactions (OERs) with a low overpotential of 391 mV and an appreciable Tafel slope of 85 mV dec^{-1}, which outperforms the benchmark catalysts IrO_2 (100.47 mV dec^{-1}) and Co_3O_4 (92 mV dec^{-1}). The magnitude of turn-over frequency (1.355×10^{-4} s^{-1}), electrochemical assessable surface area (2.4 cm^2) and faradaic

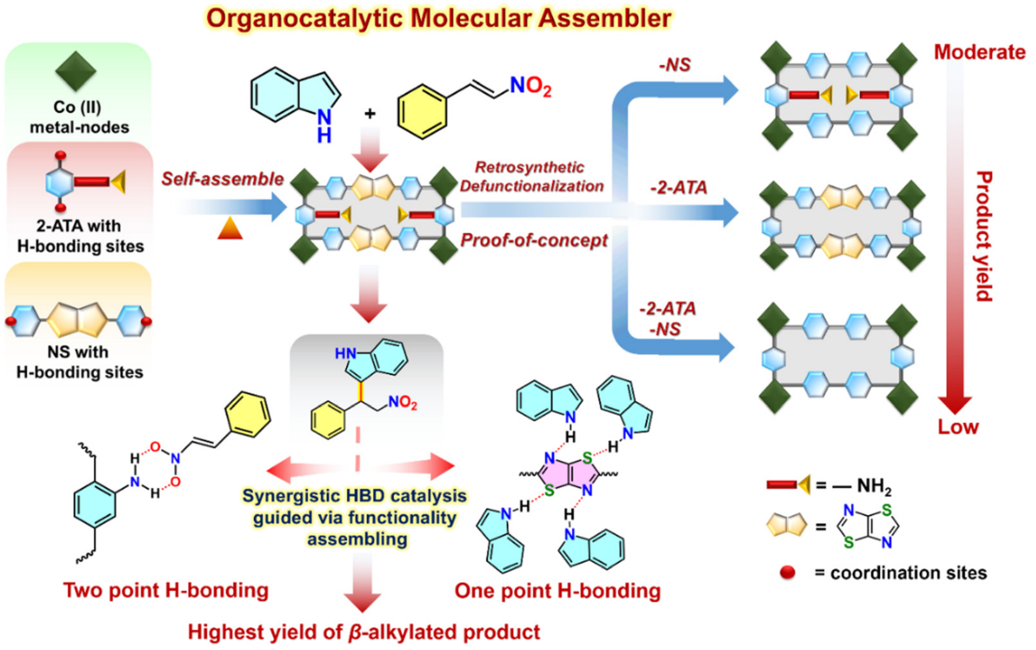

Fig. 11 Schematic illustration of the organo-catalytic molecular catassembler as a proof of concept for boosted HBD catalysis.

efficiency (94.6%) stand among best values reported in the contemporary literature, while a minor change in resistance even after 1000 CV cycles delineates this chemo-robust MOF as a proficient OER electrocatalyst. The microporous vessel delineates unique $-NH_2$-hook-mediated recyclable FC alkylation of indole and β-nitrostyrene *via* HBD catalysis under mild conditions with a broad substrate scope. For the best HBD catalysis, larger sized and sterically encumbered substrates divulge lower conversion and justify unprecedented pore-fitting-induced size selectivity. The most interesting and intriguing part of this work is the systematic rationalization of key roles of task-specific sites in OER and HBD catalysis from juxtaposing the performance of three isostructural Co(II) MOFs by a sequential functional assembly of retrosynthetically fragmented MOFs, further corroborated by a battery of experimental evidence. This novel strategy is conceptualized as an unprecedented molecular catassembler that comprehensively demonstrates the superiority of the present system. To the best of our knowledge, such molecular-engineering-driven fabrication of molecular assemblers *via* functionality-fuelled catalytic evolution is hitherto unexplored, and promises unlocking newer avenues in designing high-performance advanced materials to resolve modern-day alarming issues.

Experimental section

Synthesis of CSMCRI-20

A mixture of $Co(NO_3)_2{\cdot}6H_2O$ (8.0 mg; 0.027 mmol), 2-amino terephthalic acid (2-ATA) (5.5 mg; 0.03 mmol) and 2,5-di(pyridin-4-yl)thiazolo[5,4-*d*]thiazole (NS) (7.5 mg; 0.025 mmol) was dissolved in a mixture of 2 mL *N*,*N*′-dimethylformamide (DMF) and 0.5 mL Millipore water. It was placed in a tightly capped 15 mL Teflon-lined glass vial and heated under autogenous pressure at 100 °C for 2 days under isothermal conditions. Red block crystals of **CSMCRI-20** (CSMCRI = Central Salt & Marine Chemicals Research Institute) were harvested in 67% yield. The crystals were washed with DMF and dried in air. Anal. calcd for $[Co(2\text{-ATA})(NS)]{\cdot}0.5DMF{\cdot}1.5H_2O$: C, 54.92; H, 4.91; N, 15.75. Found: C, 54.61; H, 4.88; N, 15.78.

Preparation of the working electrode using activated CSMCRI-20

To check the catalytic activity of activated MOFs towards electrochemical oxidation of water to oxygen, a catalytic ink was prepared by adding a binder with **20a**. The electrode was fabricated by mixing **20a** with polyvinylidenedifluoride (PVDF) and *N*-methylpyrrolidinone (NMP) by grinding and keeping the material in an oven at 80 °C for 12 h. The dried material over carbon cloth as the conducting substance was used as the catalyst to study the OER activity in an alkaline medium (1 M KOH, pH: 14). The calculated catalyst loading was 1.2 mg cm^{-2}. To check the electrocatalytic performances of other three frameworks, a similar protocol was followed.

General procedure for HBD catalysis

β-nitrostyrene (15 mg, 0.1 mmol), indole (17.5 mg, 0.15 mmol), and 9 mol% catalyst were mixed in 5 mL round-bottom screw cap vials. To this, 500 μL of DCM was added and the reaction mixture was stirred at 60 °C for different time periods, as per Table 1. After the reaction mixture was cooled to room temperature, the catalyst was centrifuged and separated. The solvent was evaporated under vacuum to get a final product. The product was analysed by ^1H NMR ($CDCl_3$). A similar procedure was adapted for the other three frameworks to proceed HBD catalysis.

Data availability

All data supporting this study are available in the manuscript and ESI.†

Author contributions

Ranadip Goswami: conceptualization, methodology, formal analysis, data curation, writing – original draft. Arun karmakar: methodology, formal analysis, data curation. Sonal Rajput: formal analysis, validation, writing – review & editing. Manpreet Singh: writing – review & editing. Dr Subrata Kundu: review, funding acquisition editing & supervision. Dr Subhadip Neogi: conceptualization, funding acquisition, review, editing & supervision.

Conflicts of interest

The authors declare no competing financial interest.

Acknowledgements

S. N. acknowledges DST-SERB (Grant no. CRG/2021/002529) and R. G. acknowledges CSIR, New Delhi for SRF (CSIR Grant no: 31/028(0281)/2020-EMR-I). A. K. acknowledges UGC for the SRF. S. K. acknowledges DST for Hydrogen and Fuel Cell research funding (DST/TMD/HFC/2K18/60 on 7-10-2019, having CSIR-CECRI OM number 18-29-03/(31/19)-TTBD-CSIR-CECRI on 24/10/2019). S. R acknowledges CSIR (grant no. MLP-0054). M. S. thanks UGC, Delhi, for providing a senior research fellowship. Analytical support from AESD & CIF (CSMCRI) is greatly acknowledged. CSMCRI Communication No. 156/2022.

Notes and references

1 V. Balzani, A. Credi, F. M. Raymo and J. F. Stoddart, Artificial Molecular Machines, *Angew. Chem., Int. Ed.*, 2000, **39**, 3348–3391.

2 A. Ghosh, I. Paul and M. Schmittel, Multitasking with Chemical Fuel: Dissipative Formation of a Pseudorotaxane Rotor from Five Distinct Components, *J. Am. Chem. Soc.*, 2021, **143**, 5319–5323.

3 C. Biagini, S. D. Fielden, D. A. Leigh, F. Schaufelberger, S. Di Stefano and D. J. A. C. Thomas, Dissipative catalysis with a molecular machine, *Angew. Chem., Int. Ed.*, 2019, **131**, 9981–9985.

4 S. Anantharaj, S. R. Ede, K. Sakthikumar, K. Karthick, S. Mishra and S. Kundu, Recent Trends and Perspectives in Electrochemical Water Splitting with an Emphasis on Sulfide, Selenide, and Phosphide Catalysts of Fe, Co, and Ni: A Review, *ACS Catal.*, 2016, **6**, 8069–8097.

5 J.-J. Duan, Z. Han, R.-L. Zhang, J.-J. Feng, L. Zhang, Q.-L. Zhang and A.-J. Wang, Iron, Manganese Co-Doped Ni_3S_2 Nanoflowers *in Situ* Assembled by Ultrathin Nanosheets as a Robust Electrocatalyst for Oxygen Evolution Reaction, *J. Colloid Interface Sci.*, 2021, **588**, 248–256.

6 T. Kumar, A. Karmakar, A. Halder and R. R. Koner, Ni(II)-Based Coordination Polymer with Pi-Conjugated Organic Linker as Catalyst for Oxygen Evolution Reaction Activity, *Energy Fuels*, 2022, **36**, 2722–2730.

7 S. Maity, D. K. Singh, D. Bhutani, S. Prasad, U. V. Waghmare, S. Sampath and E. Muthusamy, High Surface Area NiCoP Nanostructure as Efficient Water Splitting Electrocatalyst for the Oxygen Evolution Reaction, *Mater. Res. Bull.*, 2021, **140**, 111312.

8 Y. Qian, I. A. Khan and D. Zhao, Electrocatalysts Derived from Metal–Organic Frameworks for Oxygen Reduction and Evolution Reactions in Aqueous Media, *Small*, 2017, **13**, 1701143.

9 Y.-P. Chen, S.-Y. Lin, R.-M. Sun, A.-J. Wang, L. Zhang, X. Ma and J.-J. Feng, FeCo/FeCoP Encapsulated in N, Mn-Codoped Three-Dimensional Fluffy Porous Carbon Nanostructures as Highly Efficient Bifunctional Electrocatalyst with Multi-Components Synergistic Catalysis for Ultra-Stable Rechargeable Zn-Air Batteries, *J. Colloid Interface Sci.*, 2022, **605**, 451–462.

10 C. Chen, Z. Yang, W. Liang, H. Yan, Y. Tuo, Y. Li, Y. Zhou and J. Zhang, Ultra-Small Co/CoO_x Nanoparticles Dispersed on N-Doped Carbon Nanosheets For Highly Efficient Electrocatalytic Oxygen Evolution Reaction, *J. Energy Chem.*, 2021, **55**, 345–354.

11 N. Liu, Q. Zhang and J. Guan, A Binuclear Co-Based Metal–Organic Framework Towards Efficient Oxygen Evolution Reaction, *Chem. Commun.*, 2021, **57**, 5016–5019.

12 W. Cheng, Z.-P. Wu, D. Luan, S.-Q. Zang and X. W. Lou, Synergetic Cobalt-Copper-Based Bimetal–Organic Framework Nanoboxes toward Efficient Electrochemical Oxygen Evolution, *Angew. Chem., Int. Ed.*, 2021, **60**, 26397–26402.

13 R. Goswami, B. D. Bankar, S. Rajput, N. Seal, R. S. Pillai, A. V. Biradar and S. Neogi, *In Situ* Fabricated MOF–Cellulose Composite as an Advanced ROS Deactivator-Convertor: Fluoroswitchable Bi-Phasic Tweezers for Free Chlorine Detoxification and Size-Exclusive Catalytic Insertion of Aqueous H_2O_2, *J. Mater. Chem. A*, 2022, **10**, 4316–4332.

14 R. Goswami, S. Das, N. Seal, B. Pathak and S. Neogi, High-Performance Water Harvester Framework for Triphasic and Synchronous Detection of Assorted Organotoxins with Site-Memory-Reliant Security Encryption *via* pH-Triggered Fluoroswitching, *ACS Appl. Mater. Interfaces*, 2021, **13**, 34012–34026.

15 N. Seal, A. S. Palakkal, M. Singh, R. Goswami, R. S. Pillai and S. Neogi, Chemically Robust and Bifunctional Co(II)-Framework for Trace Detection of Assorted Organo-toxins and Highly Cooperative Deacetalization–Knoevenagel Condensation with Pore-Fitting-Induced Size-Selectivity, *ACS Appl. Mater. Interfaces*, 2021, **13**, 28378–28389.

16 A. Goswami, D. Ghosh, V. V. Chernyshev, A. Dey, D. Pradhan and K. Biradha, 2D MOFs with Ni(II), Cu(II), and Co(II) as Efficient Oxygen Evolution Electrocatalysts: Rationalization of Catalytic Performance *vs.* Structure of the MOFs and Potential of the Redox Couples, *ACS Appl. Mater. Interfaces*, 2020, **12**, 33679–33689.

17 N. Seal and S. Neogi, Intrinsic-Unsaturation-Enriched Biporous and Chemorobust Cu(II) Framework for Efficient Catalytic CO_2 Fixation and Pore-Fitting Actuated Size-Exclusive Hantzsch Condensation with Mechanistic Validation, *ACS Appl. Mater. Interfaces*, 2021, **13**, 55123–55135.

18 G.-D. Wang, Y.-Z. Li, W.-J. Shi, L. Hou, Y.-Y. Wang and Z. Zhu, One-Step C_2H_4 Purification from Ternary C_2H_6/C_2H_4/C_2H_2 Mixtures by a Robust Metal–Organic Framework with Customized Pore Environment, *Angew. Chem., Int. Ed.*, 2022, **61**, e202205427.

19 S. Payra, N. Devaraj, K. Tarafder and S. Roy, Unprecedented Electroreduction of CO_2 over Metal Organic Framework-Derived Intermetallic Nano-Alloy Cu0.85Ni0.15/C, *ACS Appl. Energy Mater.*, 2022, **5**, 4945–4955.

20 K. Ge, S. Sun, Y. Zhao, K. Yang, S. Wang, Z. Zhang, J. Cao, Y. Yang, Y. Zhang, M. Pan and L. Zhu, Facile Synthesis of Two-Dimensional Iron/Cobalt Metal–Organic Framework for Efficient Oxygen Evolution Electrocatalysis, *Angew. Chem., Int. Ed.*, 2021, **60**, 12097–12102.

21 S. Bhattacharyya and T. K. Maji, Multi-Dimensional Metal–Organic Frameworks Based On Mixed Linkers: Interplay Between Structural Flexibility and Functionality, *Coord. Chem. Rev.*, 2022, **469**, 214645.

22 J. Li, P. M. Bhatt, J. Li, M. Eddaoudi and Y. Liu, Recent Progress on Microfine Design of Metal–Organic Frameworks: Structure Regulation and Gas Sorption and Separation, *Adv. Mater.*, 2020, **32**, 2002563.

23 N. Seal, K. Karthick, M. Singh, S. Kundu and S. Neogi, Mixed-Ligand-Devised Anionic MOF with Divergent open Co(II)-Nodes as Chemo-Resistant, Bi-Functional Material for Electrochemical Water Oxidation and Mild-Condition Tandem CO_2 Fixation, *Chem. Eng. J.*, 2022, **429**, 132301.

24 Y. Xu, M. Kraft and R. Xu, Metal-Free Carbonaceous Electrocatalysts and Photocatalysts for Water Splitting, *Chem. Soc. Rev.*, 2016, **45**, 3039–3052.

25 S. Huang, Y. Meng, S. He, A. Goswami, Q. Wu, J. Li, S. Tong, T. Asefa and M. Wu, N-, O-, And S-Tridoped Carbon-Encapsulated Co_9S_8 Nanomaterials: Efficient Bifunctional Electrocatalysts For Overall Water Splitting, *Adv. Funct. Mater.*, 2017, **27**, 1606585.

26 X.-F. Lu, P.-Q. Liao, J.-W. Wang, J.-X. Wu, X.-W. Chen, C.-T. He, J.-P. Zhang, G.-R. Li and X.-M. Chen, An Alkaline-Stable, Metal Hydroxide Mimicking Metal–Organic Framework for Efficient Electrocatalytic Oxygen Evolution, *J. Am. Chem. Soc.*, 2016, **138**, 8336–8339.

27 P. H. Ling, X. N. Zang, C. H. Qian and F. Gao, A Metal–Organic Framework with Multienzyme Activity as a Biosensing Platform for Real-Time Electrochemical Detection of Nitric Oxide and Hydrogen Peroxide, *Analyst*, 2021, **146**, 2609–2616.

28 P. R. Schreiner, Metal-Free Organocatalysis through Explicit Hydrogen Bonding Interactions, *Chem. Soc. Rev.*, 2003, **32**, 289–296.

29 J. V. Alegre-Requena, E. Marques-Lopez, R. P. Herrera and D. D. Diaz, Metal–Organic Frameworks (MOFs) Bring New Life to Hydrogen-Bonding Organocatalysts in Confined Spaces, *CrystEngComm*, 2016, **18**, 3985–3995.

30 I. Smajlagic, B. Carlson, N. Rosano, H. Foy and T. Dudding, Charge-enhanced thiourea catalysts as hydrogen bond donors for Friedel–Crafts Alkylations, *Tetrahedron*, 2019, **75**, 130757.

31 M. Singh and S. Neogi, Urea-Engineering Mediated Hydrogen-Bond Donating Friedel–Crafts Alkylation of Indoles and Nitroalkenes In a Dual-Functionalized Microporous Metal–Organic Framework with High Recyclability and Pore-Fitting-Induced Size-Selectivity, *Inorg. Chem. Front.*, 2022, **9**, 1897–1911.

32 E. A. Hall, L. R. Redfern, M. H. Wang and K. A. Scheidt, Lewis Acid Activation of a Hydrogen Bond Donor Metal–Organic Framework for Catalysis, *ACS Catal.*, 2016, **6**, 3248–3252.

33 C. Zhu, Q. Mao, D. Li, C. Li, Y. Zhou, X. Wu, Y. Luo and Y. Li, A Readily Available Urea Based MOF That Act as a Highly Active Heterogeneous Catalyst for Friedel-Crafts Reaction of Indoles and Nitrostryenes, *Catal. Commun.*, 2018, **104**, 123–127.

34 J. M. Roberts, B. M. Fini, A. A. Sarjeant, O. K. Farha, J. T. Hupp and K. A. Scheidt, Urea Metal–Organic Frameworks as Effective and Size-Selective Hydrogen-Bond Catalysts, *J. Am. Chem. Soc.*, 2012, **134**, 3334–3337.

35 D. Markad and S. K. Mandal, Design of a Primary-Amide-Functionalized Highly Efficient and Recyclable Hydrogen-Bond-Donating Heterogeneous Catalyst for the Friedel–Crafts Alkylation of Indoles with beta-Nitrostyrenes, *ACS Catal.*, 2019, **9**, 3165–3173.

36 C. M. McGuirk, M. J. Katz, C. L. Stern, A. A. Sarjeant, J. T. Hupp, O. K. Farha and C. A. Mirkin, Turning On Catalysis: Incorporation of a Hydrogen-Bond-Donating Squaramide Moiety into a Zr Metal–Organic Framework, *J. Am. Chem. Soc.*, 2015, **137**, 919–925.

37 B. D. Bankar, J. H. Advani and A. V. Biradar, Exceptional Catalytic Activity of Cu–Zn/ZrO_2 Mixed Metal Oxide towards the Oxidation Reaction, *ChemistrySelect*, 2021, **6**, 3814–3821.

38 P. C. Rao and S. Mandal, Friedel-Crafts Alkylation of Indoles with Nitroalkenes through Hydrogen-Bond-Donating Metal–Organic Framework, *ChemCatChem*, 2017, **9**, 1172–1176.

39 R. Herges, Molecular Assemblers: Molecular Machines Performing Chemical Synthesis, *Chem. Sci.*, 2020, **11**, 9048–9055.

40 V. A. Blatov, M. O'Keeffe and D. M. Proserpio, Vertex-, Face-, Point-, Schlafli-, and Delaney-symbols in Nets, Polyhedra and Tilings: Recommended Terminology, *CrystEngComm*, 2010, **12**, 44–48.

41 A. L. Spek, Single-Crystal Structure Validation with the program PLATON, *J. Appl. Crystallogr.*, 2003, **36**, 7–13.

42 P. Sharma, R. Goswami, S. Negi and V. K. Shahi, Devising Ultra-Robust Mixed-Matrix Membrane Separators Using Functionalized Mof–Poly(Phenylene Oxide) For High-Performance Vanadium Redox Flow Batteries, *J. Mater. Chem. A*, 2022, **10**, 11150–11162.

43 R. Goswami, K. Karthick, S. Das, S. Rajput, N. Seal, B. Pathak, S. Kundu and S. Neogi, Brønsted Acid-Functionalized Ionic Co(II) Framework: A Tailored Vessel for Electrocatalytic Oxygen Evolution and Size-Exclusive Optical Speciation of Biothiols, *ACS Appl. Mater. Interfaces*, 2022, **14**, 29773–29787.

44 S. Bag, K. Roy, C. S. Gopinath and C. R. Raj, Facile Single-Step Synthesis of Nitrogen-Doped Reduced Graphene Oxide-Mn_3O_4 Hybrid Functional Material for the Electrocatalytic

Reduction of Oxygen, *ACS Appl. Mater. Interfaces*, 2014, **6**, 2692–2699.

45 H. B. Aiyappa, J. Thote, D. B. Shinde, R. Banerjee and S. Kurungot, Cobalt-Modified Covalent Organic Framework as a Robust Water Oxidation Electrocatalyst, *Chem. Mater.*, 2016, **28**, 4375–4379.

46 L. Ai, X. Gao and J. Jiang, *In Situ* Synthesis of Cobalt Stabilized on Macroscopic Biopolymer Hydrogel as Economical and Recyclable Catalyst for Hydrogen Generation from Sodium Borohydride Hydrolysis, *J. Power Sources*, 2014, **257**, 213–220.

47 S. Anantharaj, S. R. Ede, K. Karthick, S. Sam Sankar, K. Sangeetha, P. E. Karthik and S. Kundu, Precision and Correctness in the Evaluation of Electrocatalytic Water Splitting: Revisiting Activity Parameters with a Critical Assessment, *Energy Environ. Sci.*, 2018, **11**, 744–771.

48 X. Zhou, X. Shen, Z. Xia, Z. Zhang, J. Li, Y. Ma and Y. Qu, Hollow Fluffy Co_3O_4 Cages as Efficient Electroactive Materials for Supercapacitors and Oxygen Evolution Reaction, *ACS Appl. Mater. Interfaces*, 2015, **7**, 20322–20331.

49 C. Zhang, C. Zhang, Y. Xie, J.-W. Su, X. He, J. D. Demaree, M. H. Griep, J. L. Atwood and J. Lin, A Supramolecular Coordination-Polymer-Derived Electrocatalyst for the Oxygen Evolution Reaction, *Chem. – Eur. J.*, 2019, **25**, 4036–4039.

50 J. Jiang, L. Huang, X. Liu and L. Ai, Bioinspired Cobalt–Citrate Metal–Organic Framework as an Efficient Electrocatalyst for Water Oxidation, *ACS Appl. Mater. Interfaces*, 2017, **9**, 7193–7201.

51 H. Jia, Y. Yao, J. Zhao, Y. Gao, Z. Luo and P. Du, A Novel Two-Dimensional Nickel Phthalocyanine-Based Metal–Organic Framework for Highly Efficient Water Oxidation Catalysis, *J. Mater. Chem. A*, 2018, **6**, 1188–1195.

52 Z. Yan, H. Sun, X. Chen, H. Liu, Y. Zhao, H. Li, W. Xie, F. Cheng and J. Chen, Anion Insertion Enhanced Electrodeposition of Robust Metal Hydroxide/Oxide Electrodes for Oxygen Evolution, *Nat. Commun.*, 2018, **9**, 2373.

53 Y.-N. Zhou, M.-X. Li, S.-Y. Dou, H.-Y. Wang, B. Dong, H.-J. Liu, H.-Y. Zhao, F.-L. Wang, J.-F. Yu and Y.-M. Chai, Promoting Oxygen Evolution by Deep Reconstruction *via* Dynamic Migration of Fluorine Anions, *ACS Appl. Mater. Interfaces*, 2021, **13**, 34438–34446.

54 B. Parmar, P. Patel, R. S. Pillai, R. K. Tak, R. I. Kureshy, N.-U. H. Khan and E. Suresh, Cycloaddition of CO_2 with an Epoxide-Bearing Oxindole Scaffold by a Metal–Organic Framework-Based Heterogeneous Catalyst under Ambient Conditions, *Inorg. Chem.*, 2019, **58**, 10084–10096.

55 F. Song, M. M. Busch, B. Lassalle-Kaiser, C.-S. Hsu, E. Petkucheva, M. Bensimon, H. M. Chen, C. Corminboeuf and X. Hu, An Unconventional Iron Nickel Catalyst for the Oxygen Evolution Reaction, *ACS Cent. Sci.*, 2019, **5**, 558–568.

56 E. Fabbri and T. J. Schmidt, Oxygen Evolution Reaction—The Enigma in Water Electrolysis, *ACS Catal.*, 2018, **8**, 9765–9774.

57 K. E. Drexler, Drexler and Smalley Make The Case for and Against'molecular Assemblers', *Chem. Eng. News*, 2003, **81**, 1.

58 Y. Wang, H.-X. Lin, L. Chen, S.-Y. Ding, Z.-C. Lei, D.-Y. Liu, X.-Y. Cao, H.-J. Liang, Y.-B. Jiang and Z.-Q. Tian, What Molecular Assembly can Learn From Catalytic Chemistry, *Chem. Soc. Rev.*, 2014, **43**, 399–411.

59 J. Tao, M.-L. Tong and X.-M. Chen, Hydrothermal Synthesis and Crystal Structures of Three-Dimensional Co-ordination Frameworks Constructed with Mixed Terephthalate (tp) and 4,4′-bipyridine (4,4′-bipy) ligands: [M(tp)(4,4′-bipy)] (M = Co^{II}, Cd^{II} or Zn^{II}), *J. Chem. Soc., Dalton Trans.*, 2000, 3669–3674.

60 X.-F. Wang, Y.-B. Zhang and W. Xue, From Nonporous to Porous Doubly-Pillared-Layer Framework: Control over Interpenetration *via* Shape Alteration of Layer Apertures, *Cryst. Growth Des.*, 2012, **12**, 1626–1631.

61 Z.-W. Zhai, S.-H. Yang, M. Cao, L.-K. Li, C.-X. Du and S.-Q. Zang, Rational Design of Three Two-Fold Interpenetrated Metal–Organic Frameworks: Luminescent Zn/Cd-Metal–Organic Frameworks for Detection of 2,4,6-Trinitrophenol and Nitrofurazone in the Aqueous Phase, *Cryst. Growth Des.*, 2018, **18**, 7173–7182.